Journal of Power Sources 196 (2011) 3461–3469

Contents lists available at ScienceDirect

Journal of Power Sources

journal homepage: www.elsevier.com/locate/jpowsour

Influence of rare-earth doping on the microstructure and conductivity of $BaCe_{0.9}Ln_{0.1}O_{3-\delta}$ proton conductors

M. Amsif[a], D. Marrero-Lopez[b,*], J.C. Ruiz-Morales[a], S.N. Savvin[a], M. Gabás[b], P. Nunez[a,*]

[a] Dpto. de Química Inorgánica, Universidad de la Laguna, 38200-Tenerife, Spain
[b] Dpto. de Física Aplicada I, Laboratorio de Materiales y Superficies (Unidad Asociada al C.S.I.C.) Universidad de Málaga, 29071-Málaga, Spain

ARTICLE INFO

Article history:
Received 8 October 2010
Received in revised form
18 November 2010
Accepted 20 November 2010
Available online 13 December 2010

Keywords:
Proton conductor
Barium cerate
Rare-earth
Freeze drying synthesis
Electrochemical measurement

ABSTRACT

Doped barium cerates $BaCe_{0.9}Ln_{0.1}O_{3-\delta}$ containing earth-rare dopants with different ionic radii, Ln = La, Nd, Sm, Gd, Yb, Tb and Y, have been investigated as candidate materials for fuel cells and other electrochemical applications. The synthesis of these materials was performed using a precursor method based on freeze-drying, which allows a precise control of the homogeneity of the ceramic powders. Dense ceramic pellets were obtained at 1400 °C under identical sintering conditions. The microstructure of the ceramics exhibits similar features with relative density higher than 95% and the grain size decreasing as the ionic radius of the dopant decreases. Impedance spectroscopy measurements were performed to study separately the different contributions to the total conductivity. The bulk, grain boundary and total conductivities depend on the ionic radius of the dopant, reaching a maximum for Gd-doped samples with a value of 0.02 S cm^{-1} for the total conductivity at 600 °C.

1. Introduction

Perovskite-type oxides based on $BaCeO_3$ exhibit high proton conductivity at intermediate temperatures, being of interest for different electrochemical applications [1–5]. Proton-conducting oxides can be used as electrolyte for intermediate temperature fuel cells (<600 °C) [6–8], with several advantages over their oxide ion-conducting counterparts. The oxide ion-conducting fuel cell produces water vapor on the anode side, which lowers the cell voltage. This further reduces the fuel utilization and requires considerable fuel circulation. In contrast, a proton-conducting fuel cell produces water at the cathode side while the fuel at the anode stays undiluted by water, increasing notably the fuel utilization and keeping a high cell voltage. Furthermore, $BaCeO_3$-based electrolytes exhibit higher conductivity than commonly used oxide-ion electrolytes based on ZrO_2, CeO_2 and $LaGaO_3$ and offer the additional possibility of reducing the operating temperature down to 500 °C with thin electrolyte layers [9].

The conducting properties of the acceptor-doped $BaCeO_3$ have been widely investigated [10–14]. Oxygen vacancies are introduced into perovskite structure by partial replacement of cerium by: Y^{3+}, Yb^{3+}, Gd^{3+}, Nd^{3+}, etc. [15–21]. The proton conduction in these materials occurs either via the hydration of oxygen vacancies after the material is exposed to water-containing atmospheres and/or by reduction of oxide ions in the lattice [11]. Proton conductivity is predominant at low temperature, whereas oxide ion conductivity is the main contribution at high temperature [19,20]. In addition, n-type and p-type electronic conductivities are also observed at high temperature, limiting the application of cerates as electrolyte materials above 700 °C.

The total conductivity of $BaCe_{1-x}M_xO_{3-\delta}$ depends on the nature of the dopant cation M and its content *x*, since both factors alter lattice cell parameters and degree of the lattice distortion, which affect the mobility of ions. Different relationships have been proposed to describe this dependence in terms of a critical radius, which minimizes the changes in the lattice parameters of the pure barium cerate [15].

The grain interior (bulk) conductivity of ceramic electrolytes often determines the overall electrical properties at high temperatures; however the grain boundary contribution is significant in the intermediate and low temperature range. The properties of the grain boundary are known to be strongly affected by the ceramic processing conditions and microstructure and it can exert a predominant effect on the properties of the ceramic materials. Thus, the optimisation of ceramic materials should not only be based on the search of the most promising phase composition, but also requires a detailed study of the relationship between ceramic processing conditions and its microstructure.

The main synthesis route used in the preparation of $BaCeO_3$ is the solid state ceramic method, which requires firing temperatures as high as 1600 °C to obtain both a single phase and dense samples

* Corresponding authors. Tel.: +34 922318501, fax: +34 922318461.
E-mail addresses: damarre@uma.es (D. Marrero-Lopez), pnunez@ull.es (P. Nunez).

0378-7753/$ – see front matter © 2010 Elsevier B.V. All rights reserved.
doi:10.1016/j.jpowsour.2010.11.120

Table 1
Structural and microstructural parameters for $BaCe_{0.9}Gd_{0.1}O_{3-\delta}$ series.

Ln	V (Å^3)	R_i (Å)	Tolerance factor (t)	Free volume V_f (Å^3)	D_g (μm)	Relative density (%)
La	341.90	1.032	0.9307	30.59	1.5	95
Nd	341.25	0.983	0.9329	30.45	1.4	96
Sm	341.15	0.958	0.9340	30.44	1.3	100
Gd	340.80	0.938	0.9348	30.36	1.2	98
Y	340.23	0.900	0.9363	30.23	1.1	95
Yb	340.80	0.868	0.9377	30.21	1.0	98
$Tb^{4+,3+}$	339.40	–	–	–	2.0	91

[21]. This method has several disadvantages, such as formation of undesirable phases, poor chemical homogeneity and large grain ceramic sizes, which negatively affect the mechanical performance. In addition, evaporation of BaO has also been detected when the sintering temperature exceeds 1500 °C [22,23], thus reducing the sintering temperature is particularly important for these materials.

An alternative preparation method based on freeze-drying precursor route was recently used to obtain powders of $BaCe_{0.9}Y_{0.1}O_{3-\delta}$ [23]. This method has proved to be very efficient for obtaining stoichiometrically controlled polymetallic compounds [24,25], yielding homogeneous and very fine powder that contributes to avoid heterogeneous distribution of cations. Moreover, the differences in transport properties related to sample preparation can be avoided by using identical powder preparation and densification processes.

In the present study, the perovskite-type oxide solid solutions $BaCe_{1-x}Ln_xO_{3-\delta}$ with trivalent dopants of different ionic size (Ln = La, Nd, Sm, Gd, Yb, Tb and Y) and with fixed amount of their content ($x = 0.1$) were synthesized. The microstructure, bulk and grain boundary contributions to the total conductivity were studied under different atmospheres with the emphasis on a possible relationship between processing and microstructure.

2. Experimental

2.1. Synthesis

Powders of $BaCe_{1-x}Ln_xO_{3-\delta}$ (Ln = La, Nd, Sm, Gd, Y, Yb and Tb) were prepared by a freeze-drying method. The reactants were high purity nitrates: $Ba(NO_3)_2$ (+99% Aldrich) and $Ln(NO_3)_3{\cdot}6H_2O$ (99.99% Aldrich). These nitrates were previously studied by thermogravimetric analysis to determine the correct cation composition. Stoichiometric quantities of reactants were dissolved in distilled water and ethylenediaminetetraacetic acid (EDTA) (99.7% Aldrich) was added in a 1:1 molar ratio ligand:metal as complex agent, which is necessary to prevent precipitation. A typical preparation of 100 ml contains 15 mmol of Ba^{2+}. The pH was adjusted at 7 by adding ammonia. The solutions were flash-frozen by dropping them into liquid nitrogen in order to maintain the cation homogeneity of the starting solution, and then dehydrated using a HetoLyolab freeze-dryer for 3 days. In this way dried and amorphous precursor powders were obtained. These precursors are very hygroscopic so that they were immediately calcined at 300 °C to prevent rehydration and to produce the combustion of organic material. The precursor powders obtained in this way were calcined between 300 and 1000 °C for 1 h, in order to study the phase formation behaviour with temperature. All the thermal treatments were carried out in alumina crucibles to prevent reaction of barium with platinum crucibles.

The as-prepared oxide powders at 1000 °C, were pressed at 200 MPa into disks of 10 mm diameter and 1.5 mm thickness. All the pellets were sintered in air at 1400 °C for 4 h. The relative density of the sintered pellets was calculated from the mass, volume of the sample and theoretical density obtained from the structural analysis by Rietveld refinement (Table 1).

2.2. Structural and microstructural characterisation

Room temperature X-ray diffraction patterns (XRD) were collected with a PANalytical X'Pert diffractometer with Cu Kα radiation and the X'Celerator detector. The scans were performed in the 2θ range (15–100°) with 0.016° step for 2 h. Structure refinements were performed using the FullProf [26] and the ICSD database for the structural models [27].

X-ray photoelectron spectroscopy (XPS) spectra were recorded on a Physical Electronics PHI-5700 spectrometer equipped with Mg Kα and Al Kα X-ray sources and a hemispherical electron analyser. The data were analysed using XPSpeak 4.1 software [28]. The experimental peaks were deconvoluted into components using mixed Gaussian–Lorentzian functions.

The microstructure of the sintered pellets was observed by Scanning Electron Microscope (SEM) using a Jeol Ltd., JSM-6300. All samples were covered with a sputtered thin film of gold to avoid charging problems and to obtain better image definition. Average grain size of sintered pellets was estimated from the SEM micrographs, using the linear intercept method from at least 50 randomly lines and two different micrographs with the help of an image-analysis software [29].

2.3. Electrical characterisation

The electrical characterisation of the ceramic material was carried out by impedance spectroscopy under different dry/wet gases (air and 5% H_2–Ar). Gases were humidified using a gas-washer at a temperature of 20 °C to ensure constant water content of about 2%. Pt electrodes were deposited on each side of the sintered pellet with Pt-ink (Metalor) and then thermally treated at 800 °C for 30 min to ensure maximum conductivity and adherence. Impedance spectra were obtained using a frequency response analyser (Solartron 1260) in the 0.1 Hz to 1 MHz frequency range with an ac signal of 50–100 mV. The spectra were acquired during the cooling process between 800 and 150 °C with a dwell time of 60 min between consecutive measurements. Equivalent circuits were used to fit the spectra and to study separately the different resistive contributions (bulk and grain boundary) to the total conductivity.

Conductivity dependence as a function of oxygen partial pressure (pO_2) from 0.21 to $\sim 10^{-20}$ atm was obtained with an electrochemical cell, which consist of a YSZ tube closed at one end, with an electrochemical pump and an oxygen sensor. Before taking measurements, the pellets were kept at 700–800 °C for 5 h while the system was flushed with humidified 5% H_2–Ar gas mixture. The oxygen partial pressure was controlled using the electrochemical pump with a dc source (Yokogawa 7651) and the oxygen partial pressure inside the cell was continuously monitored by means of the oxygen sensor (voltage read by Keithley 2700 multimeter) placed close to the sample. The samples were equilibrated at each oxygen partial pressure at least for 2 h before acquiring the impedance spectra.

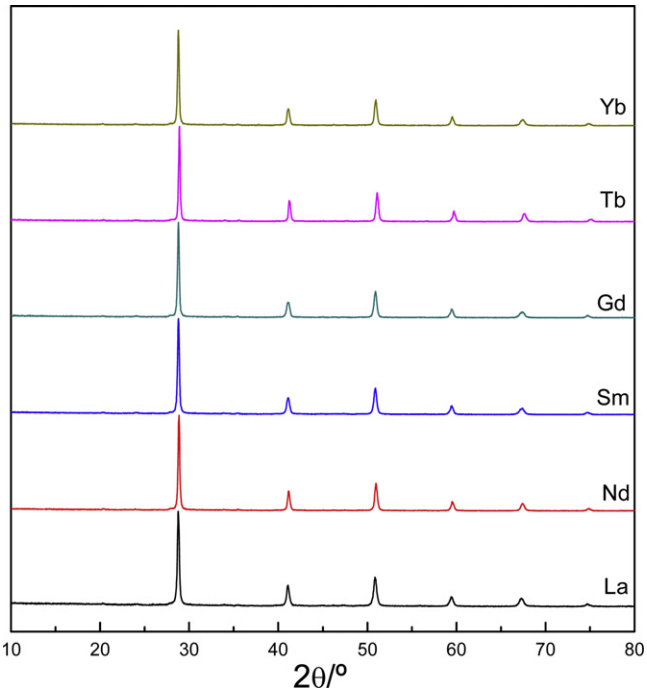

Fig. 1. XRD powder patterns of $BaCe_{0.9}Ln_{0.1}O_{3-\delta}$ (Ln = La, Nd, Sm, Gd, Tb and Yb) prepared by freeze-drying method at 1000 °C for 1 h.

3. Results and discussions

3.1. Structure

The perovskite phase crystallizes after one single thermal treatment of the precursor powders at 800 °C, although a small amount of $BaCO_3$ impurity is still detected by means of high resolution XRD. This impurity disappears after calcination at 1000 °C for 1 h. The XRD patterns corresponding to as-prepared powders at 1000 °C (Fig. 1) indicate that, in all samples, the perovskite structure is obtained and no additional phases are observed.

In order to improve crystallization of the compounds and facilitate their structural characterisation, the polycrystalline powders were pressed into pellets, calcined at 1400 °C for 4 h and then slowly cooled in air to room temperature. The XRD patterns were analysed by the Rietveld method using the structural models previously proposed in the literature (ICSD 72768) in the orthorhombic Pmcn space group.

The lattice cell volume was plotted against the ionic radii [30] of the six coordinated rare-earth dopant cation (Fig. 2a). In this figure a linear dependence is observed, which is the typical behaviour expected for a solid solution. However, this trend is not followed by Tb-doped sample, if the perovskite structure is supposed to contain only six coordinated Tb^{3+} with ionic radius of 0.90 Å. This sample was thermally treated under a continuous flux of wet diluted hydrogen (5% H_2–Ar) at 800 °C and then analysed by XRD. The cell volume changed significantly from 337.56 to 339.40 Å^3 after the thermal treatment in oxidising and reducing atmospheres respectively (Fig. 2a); however, this important volume change was not observed in the other samples. These results seem to indicate that Tb^{4+} and Tb^{3+} ions coexist simultaneously in reduced $BaCe_{0.9}Tb_{0.1}O_{3-\delta}$ sample. This issue was further confirmed by XPS and impedance spectroscopy analysis in the next sections.

It is generally assumed that lower distortion of the lattice cell and larger free volume favour the ionic conduction in perovskites. In order to correlate the structure with the transport properties, the tolerance factor and crystallographic free volume were determined.

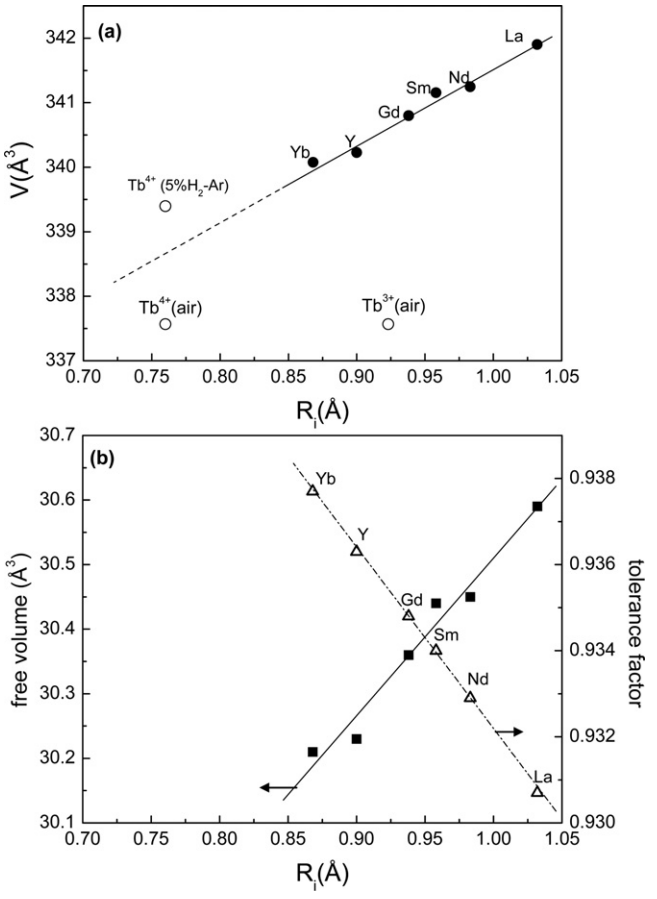

Fig. 2. (a) Variation of the unit cell volume and (b) free volume (V_f) and the tolerance factor (t) in $BaCe_{0.9}Ln_{0.1}O_{3-\delta}$ (Ln = La, Nd, Sm, Gd, Tb, Yb and Y) compounds as a function of the rare-earth ionic radius. Open circles in (a) represent the cell volume for Tb-doped sample considering only Tb^{4+} or Tb^{3+} in the structure.

The degree of distortion of ABO_3 perovskite structure is given by the Goldschmidt tolerance factor (t), defined as [31]:

$$t = \frac{r_A + r_O}{\sqrt{2}(r_B + r_O)} \quad (1)$$

where r_A and r_B are the ionic radii of the cations occupying the A and B site respectively, while r_O is the oxygen ionic radii. The tolerance factor of undoped barium cerate is 0.9376 and it decreases linearly with increasing the earth-rare ionic radius of the dopant from 0.9377 for Yb^{3+} to 0.9307 for La^{3+} (Fig. 2b). Thus, the lattice distortion of $BaCeO_3$ perovskite decreases as the ionic radius of the dopant in the B-position is getting smaller.

On the other hand, the free volume (V_f) is defined as the lattice unit cell volume minus the ionic volume of the constituent ions. As can be observed in Table 1 and Fig. 2b the free volume decreases with decreasing the ionic radius of the dopant from 30.59 Å^3 for La^{3+} to 30.21 Å^3 for Yb^{3+}.

Thus, dopants with smaller ionic radii exhibit higher tolerance factor (increasing the ionic mobility) and lower free volume (decreasing ionic mobility); and a contrary trend is observed for dopant with larger ionic radii. Hence, cations with intermediate values of free volume and tolerance factor are expected to be the best ones for optimizing the ionic conductivity in barium cerates.

3.2. XPS analysis

Several sintered pellets of $BaCe_{0.9}Ln_{0.1}O_{3-\delta}$ were exposed to oxidising and reducing atmospheres at 800 °C under a constant flow of wet air and wet 5% H_2–Ar gas mixture for 12 h. The pellet surfaces

were ground with SiC paper before XPS measurements to remove the superficial layer, because $BaCeO_3$ materials are susceptible to surface carbonation in the presence of CO_2.

It should be commented that the spectra of reduced Gd and Yb-doped samples are shifted to higher binding energies compared to the oxidised samples; and a reverse tendency is observed for Tb-doped samples (Fig. S1 and S2, Supplementary Materials). This behaviour may be explained by the different conductivity values of these samples in reducing and oxidising atmospheres as further discussed below. Gd- and Yb-doped samples exhibit larger conductivity values under oxidising conditions due to the presence of a significant p-type contribution. Conversely, Tb-doped samples have very low conductivity under oxidising condition. In this sample, Tb is in an oxidation state +4 in air and it partially reduces to Tb^{3+} under hydrogen atmosphere, increasing the oxygen vacancy concentration and enhancing considerably the ionic conductivity.

The Ba 3d core level has a quite simple spectrum in all the samples, a typical 3d doublet with FWHM of 2.0–2.1 eV and only one contribution (Fig. S1 Supplementary Materials). The Ba $3d_{5/2}$ peak shows a maximum at ~785 eV, which is higher than expected. This is probably related to the low electronic conductivity of these samples. Thus, a shift in the binding energies of ~4 eV was applied in order to ascribe the different contributions of the core levels spectra.

C 1s spectra show two separated peaks with at least five different contributions in all the samples (Fig. S2 Supplementary Materials). They have been ascribed to adventitious carbon, different C–O and C=O species and carbonates, being those corresponding to C–O and carbonates the most intense ones.

The spectra corresponding to the 4d core-level of the rare-earth dopants exhibit very low intensity. The characteristic 4d doublet of the rare-earth dopants is difficult to distinguish due to the low fraction of these cations in the samples and their very low intensity in the XPS spectra. A comparison between the spectra of reduced and oxidized samples does not reveal appreciable differences with the exception of the Tb 4d core level. In this case, the spectrum of the reduced sample shows a tiny shoulder at low energy side compared to the oxidised sample, which is associated to the presence of mixed oxidations states of Tb^{4+} and Tb^{3+} ions (not shown).

O 1s core levels show a rather complicated structure, quite similar in all the samples. Four different contributions have been considered to adequately fit the experimental spectra (Fig. 3). The

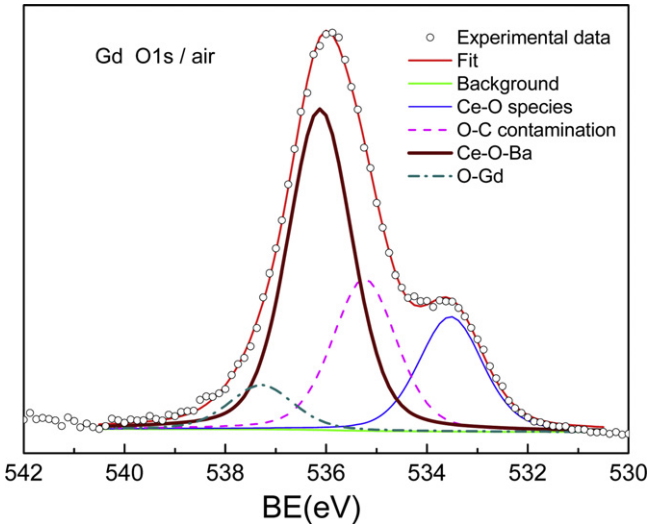

Fig. 3. XPS spectra for the O 1s core level of $BaCe_{0.9}Gd_{0.1}O_{3-\delta}$.

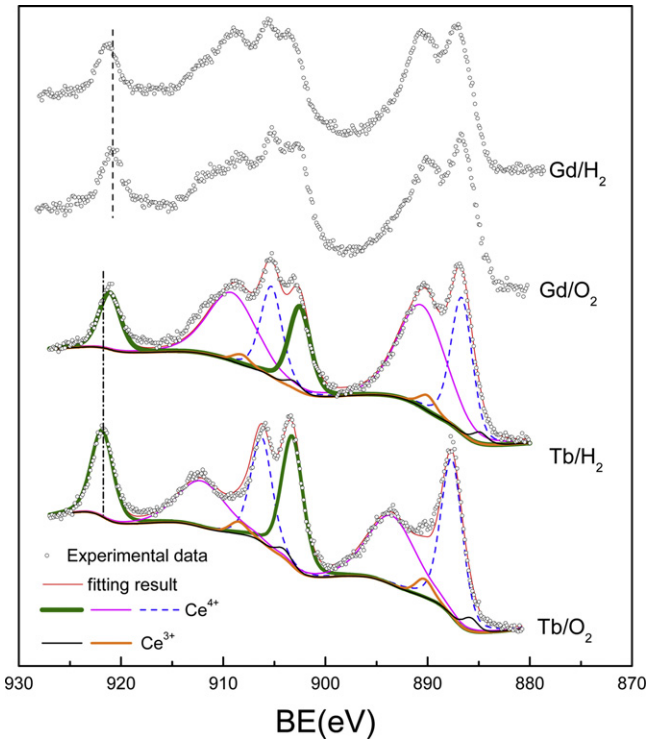

Fig. 4. XPS spectra for the Ce 3d core levels of $BaCe_{0.9}Gd_{0.1}O_{3-\delta}$ (BCG) and $BaCe_{0.9}Tb_{0.1}O_{3-\delta}$ (BCT) samples as-prepared in air and after thermal treatment under 5% H_2–Ar flow at 800 °C.

lowest binding energy contribution at 529.9 eV might be assigned to different superficial Ce-containing oxides and hydroxides [32]. The second contribution is associated to superficial oxygen contamination, such as specimens containing C–O bonds. The most intense contribution, about 45% of the total peak intensity, with a binding energy higher than those corresponding to simple metal oxides is ascribed to the oxygen belonging to the perovskite structure. Finally, a small contribution with less than 10% of the total peak intensity is observed at higher binding energies, which is probably related to Ln–O bonds of the trivalent dopant (Fig. 3).

The Ce 3d core level data show the usual multicomponent spectra due to the presence of different Ce oxidation states (Fig. 4). One would expect negligible Ce^{3+} contribution in oxidising atmospheres, however partial reduction of cerium during recording of the XPS spectra at the surface of the pellets is possible as has been previously observed [33]. It is worth mentioning that all the spectra look very similar, except that corresponding to the oxidised Tb-doped sample (Fig. 4), which exhibits the highest content of Ce^{4+}. This seems to indicate that oxidised $BaCe_{0.9}Tb_{0.1}O_{3-\delta}$ without oxygen vacancies in the structure shows lower degree of reducibility than those containing oxygen vacancies. It should be noted that a similar behaviour has been also observed in undoped and doped CeO_2 [34]. Considering also that Ce cations have different symmetry environments due to the presence of several Ce-containing compounds at the surface of the samples, such as hydroxides, there will be more than one contribution to the spectra for each oxidation state. Thus, the Ce^{3+}/Ce^{4+} fraction is difficult to determine in these compounds.

3.3. Ceramic microstructure

The microstructure of the sintered pellets was analysed as a function of the dopant type from SEM micrographs. SEM images for the different pellets sintered at 1400 °C for 4 h are shown in Fig. 5. No appreciable traces of impurities or phase segregations at

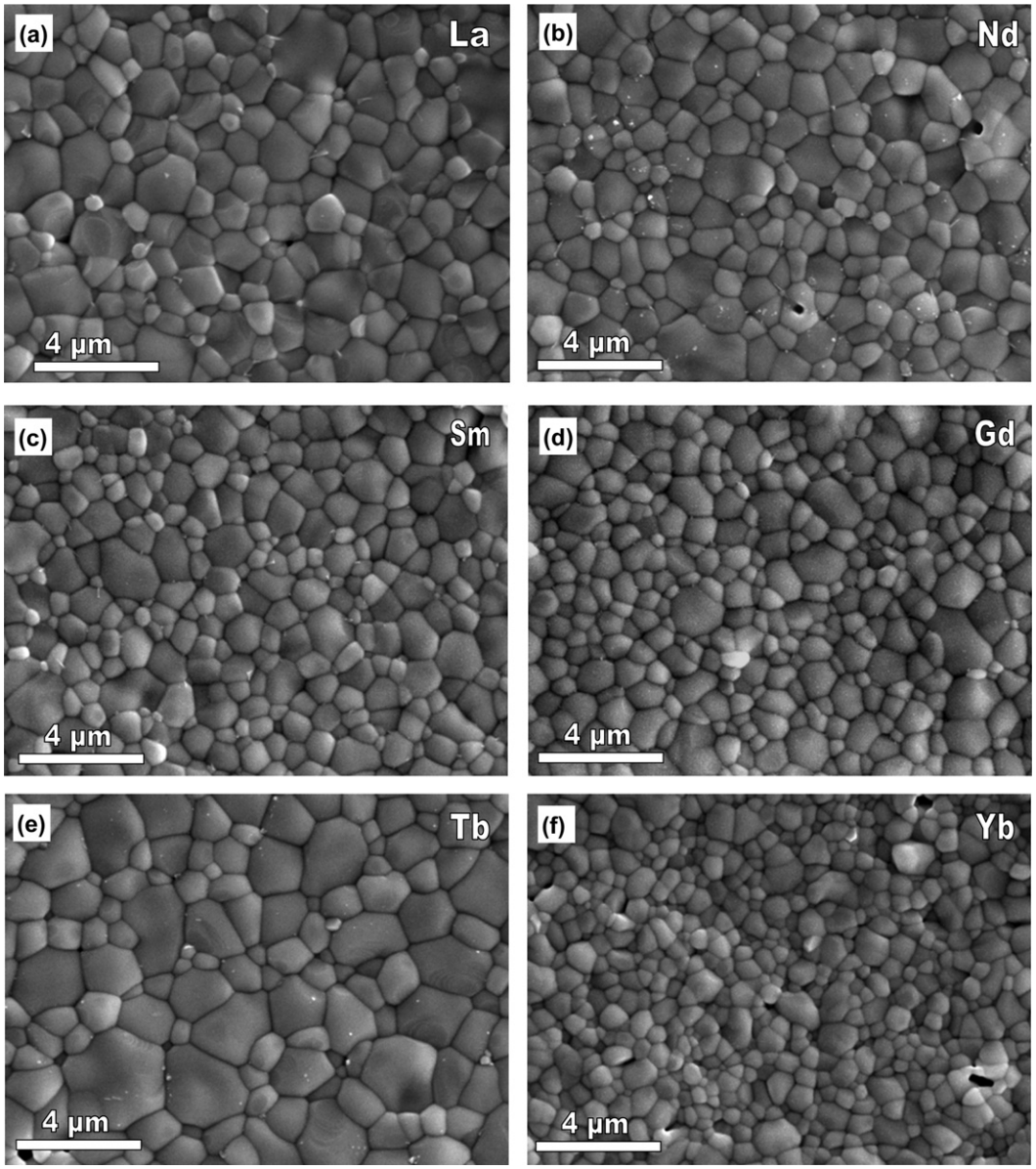

Fig. 5. SEM images of $BaCe_{0.9}Ln_{0.1}O_{3-\delta}$, Ln = (a) La, (b) Nd, (c) Sm, (d) Gd, (e) Tb and (f) Yb, pellets sintered at 1400 °C for 4 h.

the grain boundaries were found in any of the samples studied. The microstructure is well developed with well connected grains and relative density higher than 95% (Table 1). Therefore, the possible effects of the porosity on the bulk and grain boundary conduction are ruled out. In general, the different dopants do not affect significantly the microstructure of the pellets and differences are mainly observed in the average grain size. The undoped $BaCeO_3$ sample exhibits an average grain size of 2.5 μm after sintering at 1400 °C for 4 h [23], however smaller grain sizes are observed in the doped samples, which is usually ascribed to lower diffusion across the grain boundary during the sintering process. The densification process occurs in a first step and then further grain growth is observed. Both processes are generally controlled by grain boundary diffusion rather than bulk diffusion. An enrichment of the trivalent dopant at the grain boundary region, according to the space charge model [35], generates a concentration gradient between the grain interior and grain boundary that decreases the mobility of cations along the grain boundary and therefore the densification and grain growth rate decreases. A similar effect has previously been observed in other materials, such as doped-CeO_2 [36].

The variation of the average grain size with the ionic radii of the rare-earth dopant shows a linear behaviour (Fig. 6), which is almost identical to that observed in the lattice cell volume (Fig. 2a). The ceramic grain size becomes smaller as the ionic radii of the dopant decreases from 1.5 μm for La^{3+} to 1 μm for Yb^{3+} (Table 1). However, this linear relationship does not hold for Tb-doped sample sintered in air, which exhibits the largest grain size ~2 μm and comparable to the undoped one. This effect can be explained taking into account that Tb-doped samples sintered in air do not contain oxygen vacancies in their structure, because Tb is in oxidation state +4, and therefore the densification process seems to be similar to that occurring in undoped $BaCeO_3$.

3.4. Electrical characterisation

The impedance spectra of $BaCe_{0.9}Ln_{0.1}O_{3-\delta}$ recorded in air show similar features (Fig. 7) with three separated contributions ascribed to grain interior (bulk), grain boundary and electrode processes. Similar spectra were obtained in wet 5% H_2–Ar gas mixture. The results suggest an ideal equivalent circuit consisting

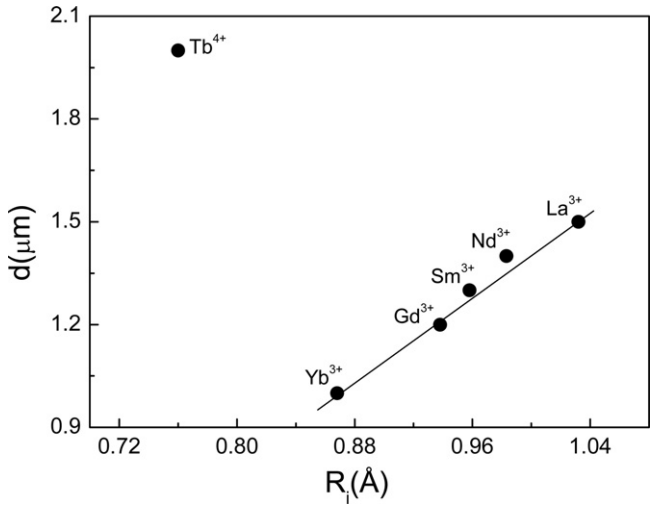

Fig. 6. Variation of the average grain size of the sintered pellets of $BaCe_{0.9}Ln_{0.1}O_{3-\delta}$ (Ln = La, Nd, Sm, Gd, Tb, Yb) series as a function of the rare-earth ionic radius.

of (RC) elements in series, although the spectra show somewhat depressed arcs. Therefore, the alternative equivalent circuit used was $(R_bQ_b)(R_{gb}Q_{gb})(Q_e)$ where the capacitors C were replaced by constant phase elements Q with impedance value of $Z_Q = 1/[Q(jw)^n]$ to achieve better results. The following parameters were fitted for each depressed arc: the resistance R_i, the pseudocapacitance Q_i and the exponential parameter n_i of bulk, grain boundary and electrode processes. These parameters are related to the angular relaxation frequency w and true capacitance C by the following relation [37]:

$$w_i = (R_iC_i)^{-1} = (R_iQ_i)^{-1/n_i} \quad (2)$$

Bulk and grain boundary contributions show typical capacitance values of pF cm^{-1} and nF cm^{-1}, respectively. Tb-doped sample displays different impedance spectra in air (Fig. 7f) with only one broad semicircle and a capacitance value of 6 pF cm^{-1}, which is associated to bulk contribution. Nevertheless, the spectra of this sample in H_2-containing atmosphere are very similar to those of the rest of the samples with three well separated contributions and much lower resistance due to $Tb^{4+} \rightarrow Tb^{3+}$ reduction and the consequent formation of oxygen vacancies that enhances the ionic conductivity.

Grain boundary and grain interior processes were studied separately in the low temperature range ($T \leq 250\,^\circ$C) were both processes are discernible. Conversely, electrode processes are dominant at higher temperatures ($T > 400\,^\circ$C) and only total conductivity was obtained. In this case, the equivalent circuit used to fit the spectra is denoted as: $LR_s(R_{e1}Q_{e1})(R_{e2}Q_{e2})$, where L is an autoinductance element, which is associated to the autoinductive effects introduced by the equipment, and R_s is a serial resistance equal to total electrolyte resistance; R_{ei} and Q_{ei} are the resistance and pseudocapacitance of each electrode process.

The relative permittivity of the bulk was estimated from the capacitance values by using the following relation:

$$\varepsilon_b = \frac{C_bL}{S\varepsilon_o} \quad (3)$$

where L and S are the thickness and electrode area of the pellets respectively and ε_o is the vacuum permittivity. A relative permittivity $\varepsilon_b \sim 40$ was obtained, which is comparable to the previously reported one $\varepsilon_b \sim 37$ [38].

The grain interior R_b and grain boundary R_{gb} resistances were used to obtain the bulk and macroscopic grain boundary conductivity, taking into account the sample geometry:

$$\sigma_i = \frac{L}{R_iS} \quad (4)$$

The values of conductivity were plotted using the Arrhenius equation:

$$\sigma = \frac{\sigma_0}{T}\exp\left(-\frac{E_a}{kT}\right) \quad (5)$$

The temperature dependence of grain interior conductivity for the different samples in wet air and wet-5% H_2–Ar gases are shown in Fig. 8a and b respectively. As can be observed the bulk conductivity depends on both the ionic radii of the dopant and the atmosphere with slightly larger values of conductivity in wet-5% H_2–Ar. The activation energy for bulk conduction, in the temperature range of 150–250 °C, decreases slightly with decreasing ionic radii of the dopant from 0.53 eV for La^{3+} to 0.46 eV for $Tb^{4,3+}$ (Table 2). In addition, the dependence of the bulk conductivity as a function of the rare-earth dopant size shows a maximum for Gd-doped samples (Fig. 9). As aforementioned, the best bulk ionic conduction in doped perovskite electrolytes corresponds to minimum lattice distortion and largest lattice free volume. The lattice distortion in doped $BaCeO_3$, defined by the tolerance factor, is lower as the ionic radius of the dopant decreases, favouring the ionic conduction. Conversely, the lattice free volume decreases with decreasing ionic radii of the dopant and thus reducing the ionic mobility. Both phenomena are involved in the bulk conduction and they can explain the maximum of the bulk conductivity observed

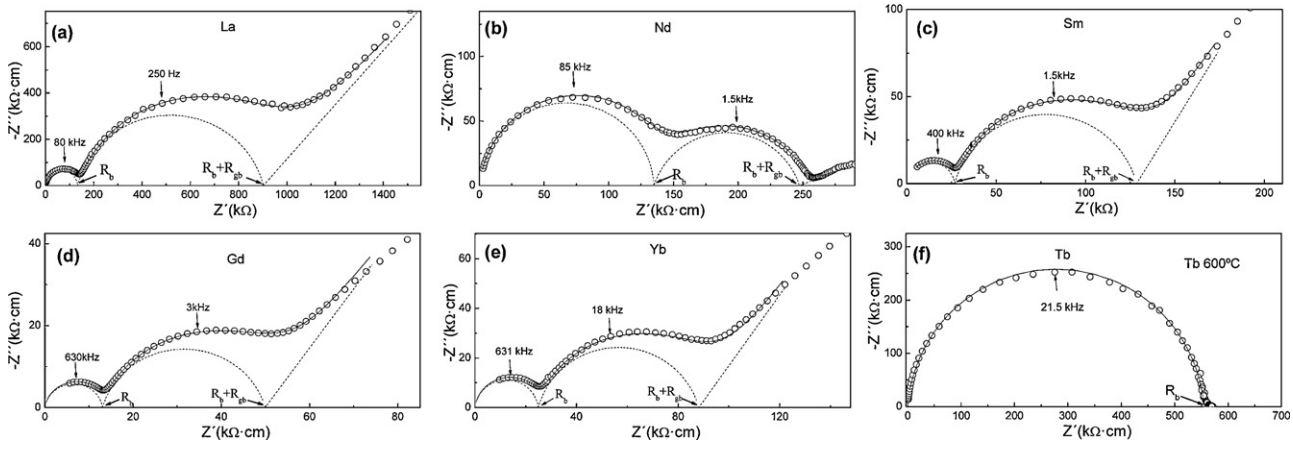

Fig. 7. Impedance spectra for $BaCe_{0.9}Ln_{0.1}O_{3-\delta}$ pellets sintered at 1400 °C for 4 h: Ln = (a) La, (b) Nd, (c) Sm, (d) Gd and (e) Yb measured at 125 °C and f) Tb at 600 °C. The solid line is curve obtained by fitting the data with equivalent circuits.

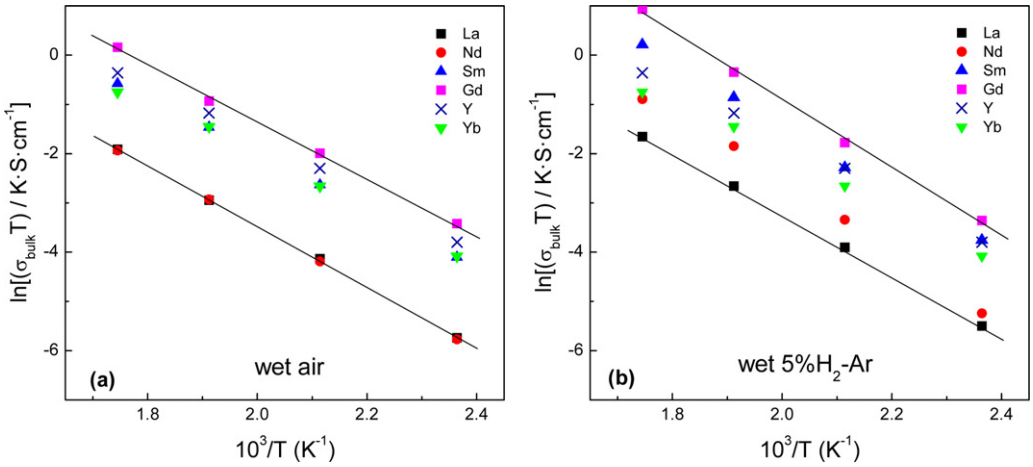

Fig. 8. Arrhenius plots of the grain interior (bulk) conductivity for $BaCe_{0.9}Ln_{0.1}O_{3-\delta}$ samples under (a) wet air and (b) wet 5% H_2–Ar gases.

Table 2
Conductivity and activation energies for the bulk and grain boundary contributions obtained from the impedance spectra in air for $BaCe_{0.9}Ln_{0.1}O_{3-\delta}$ series.

Ln	σ_{bulk} (μS cm^{-1})$^{200\,^\circ C/air}$	σ_{gb} (μS cm^{-1}), $^{200\,^\circ C/air}$	E_{bulk} (eV)^{air}	E_{gb} (eV)^{air}	δ_{gb} (nm)^{air}
La	33	0.04	0.53	0.82	4.5
Nd	36	0.22	0.53	0.75	4.6
Sm	151	0.41	0.49	0.76	5.0
Gd	289	0.61	0.49	0.72	3.2
Y	212	0.46	0.48	0.77	4.9
Yb	148	0.21	0.47	0.77	4.1
Tb	0.018	–	0.46	–	–

around Gd radius with intermediate values of t and V_f (Fig. 2b and Fig. 9).

The Arrhenius plots of the macroscopic grain-boundary resistance $L/(S \times R_{gb})$ shows a similar trend to the bulk one, reaching a maximum for Gd-doped samples (Figs. 9 and 10). The activation energies of the grain-boundary resistance are larger than those corresponding to the bulk, ranging from 0.72 to 0.82 eV and reaching the minimum value for Gd-doped sample (Table 2). The different grain boundary resistances cannot be only attributed to differences in grain sizes, since the average grain size is similar for all the samples, ranging between 1 and 2 μm. It should be considered that the grain boundary conductivity calculated using Eq.(4) is not reliable because the thickness of the grain boundary parallel to the current flow is much smaller than that of the pellet (L/S). Thus, both the grain boundary layer thickness and grain size must be considered to evaluate the microscopic grain boundary conductivity, defined as [39,40]:

$$\sigma_{gb} = \frac{L}{R_{gb}S} \times \frac{\delta_{gb}}{D} \quad (6)$$

where D is the average grain size and δ_{gb} the thickness of the grain boundary layer. The grain boundary layer widths δ_{gb} and the grain size D should be known to obtain σ_{gb} and they can be only obtained by microscopic analysis. An alternative approach to estimate the grain boundary conductivity consists in the use of the bulk and grain boundary resistances and capacitances [40]:

$$\sigma_{gb} = w_{gb}\varepsilon_o\varepsilon_{gb} \quad (7)$$

The grain boundary width δ_{gb} can be also estimated using the Eq.8, which has been obtained by combining Eqs. (6) and (7) and considering a similar value of permittivity for grain interior and grain boundary ($\varepsilon_{gb} \approx \varepsilon_b$):

$$\delta_{gb} = \frac{\varepsilon_o\varepsilon_b}{C_{gb}}\frac{DS}{L} \quad (8)$$

The estimated grain boundary widths vary between 3.2 and 4.5 nm, which are comparable to the values reported for other solid electrolytes (e.g. 1–2 nm for $Ce_{0.8}Gd_{0.2}O_{1.9}$ [41] and 3–4 nm for $Zr_{0.84}Y_{0.16}O_{1.92}$ [42]). The grain boundary widths in Table 2 have been calculated presuming a similarity of permittivity between the grain boundary and the grain interior regions, although the composition of the grain boundaries might be different depending on segregations and morphology changes, so that the values of δ_{gb} are only estimated, but they are reasonable when compared to other solid electrolytes.

The Arrhenius plots of the total conductivity in wet air and 5% H_2–Ar gas mixture are shown in Fig. 11. Similarly to the bulk conductivity, the total conductivity depends on the earth-rare dopant

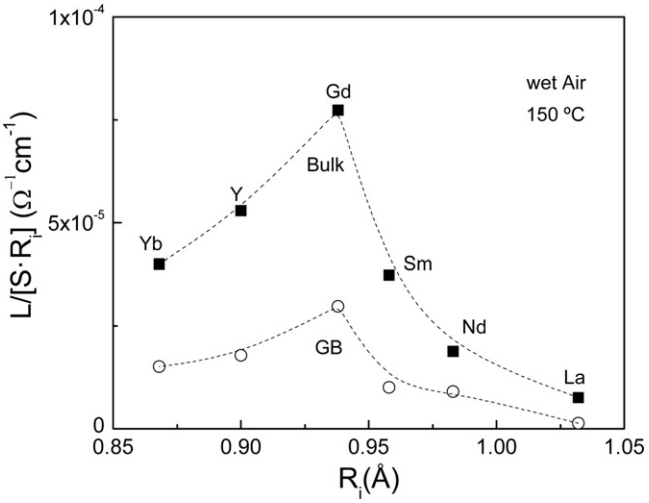

Fig. 9. Variation of the bulk conductivity and the macroscopic graing boundary (GB) resistance at 150 °C as a function of the rare-earth ionic radius.

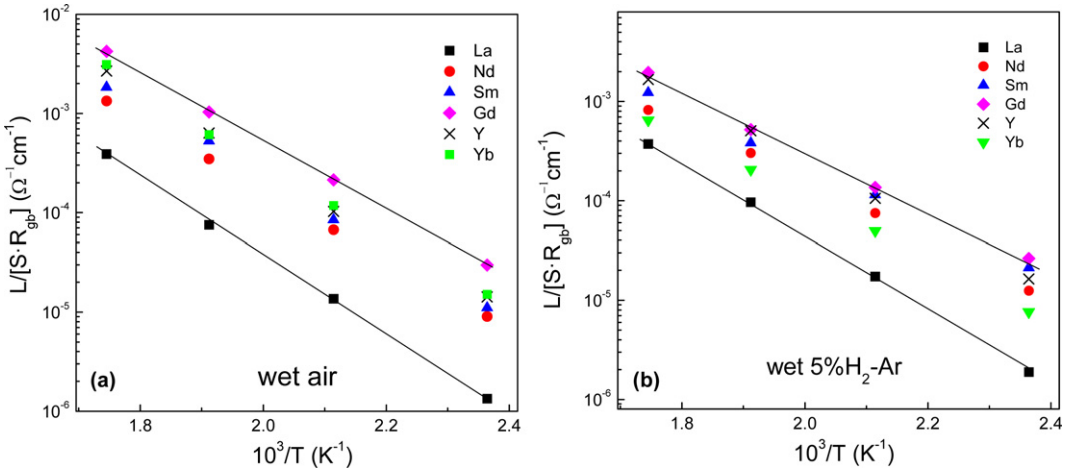

Fig. 10. Arrhenius plots of the grain boundary resistance for $BaCe_{0.9}Ln_{0.1}O_{3-\delta}$ samples under (a) wet air and (b) wet 5% H_2–Ar.

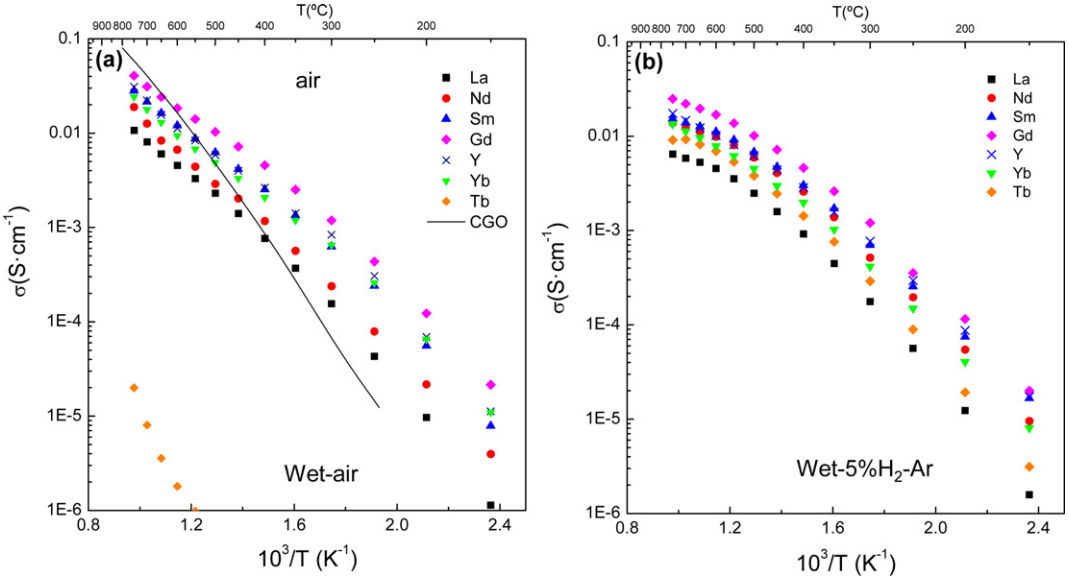

Fig. 11. Arrhenius plots of the total conductivity for $BaCe_{0.9}Ln_{0.1}O_{3-\delta}$ samples under (a) wet air and (b) wet 5% H_2–Ar.

size, the Gd-doped samples showing the highest conductivity values (Fig. 12).

It should be commented that Bonanos et al. [18] reported previously larger conductivity values in Gd-doped $BaCeO_3$ than in Y-doped $BaCeO_3$.

It is also evident from Fig. 11 that doped cerates show higher conductivity in air than in hydrogen atmosphere at the high temperature range. In air with high oxygen partial pressure, these specimens show significant p-type conduction and when water vapour or hydrogen is introduced into the atmosphere, the p-type contribution decreases compared to proton contribution.

The conductivity of all these electrolytes is substantially higher than that of the ceria-based ones (e.g. $Ce_{0.8}Gd_{0.2}O_{1.9}$) with oxide ion conduction and especially at temperatures lower than 500 °C (Fig. 11a) and therefore they are good candidates for solid oxide fuel cell applications.

The conductivity of Gd-doped sample as a function of the oxygen partial pressure is shown in Fig. 13a. The water partial pressure was kept at 0.02 atm by bubbling water at room temperature. At the high pO_2 range of 10^{-5}–0.21 atm, the conductivity increases with pO_2, indicating that the conduction mechanism includes ionic and electron–hole components. A plateau region observed

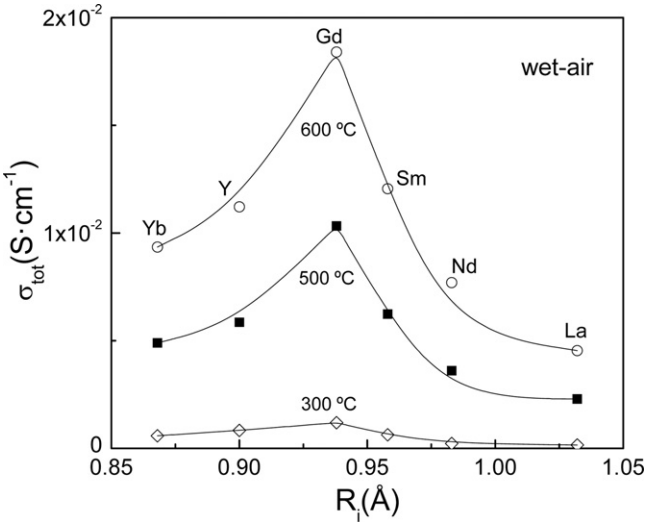

Fig. 12. Variation of the total conductivity at 300, 500 and 600 °C in $BaCe_{0.9}Ln_{0.1}O_{3-\delta}$ compounds as a function of the rare-earth radius of the dopant in wet air atmosphere.

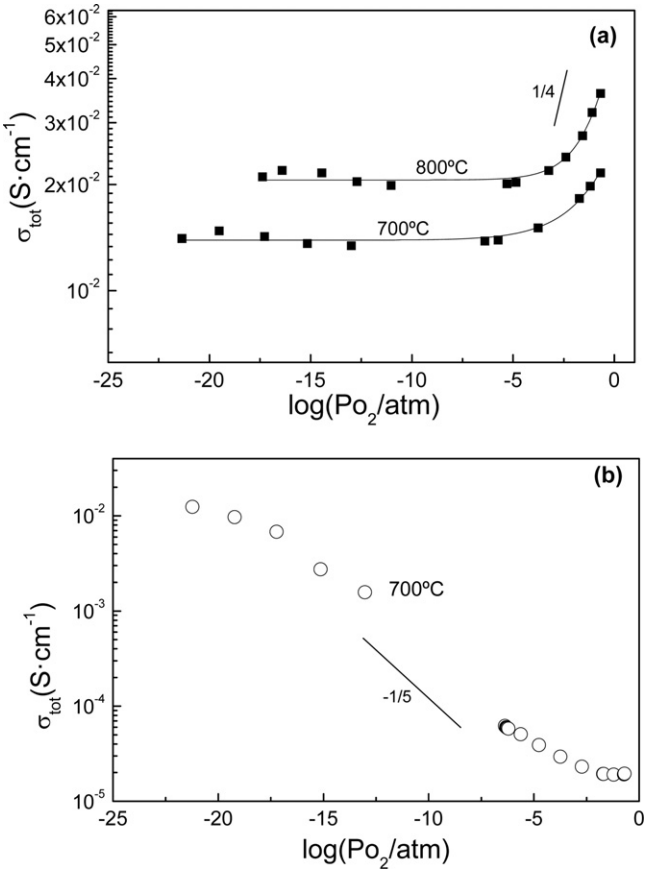

Fig. 13. Oxygen partial pressure dependence of the total conductivity at 700 and 800 °C for (a) $BaCe_{0.9}Gd_{0.1}O_{3-\delta}$ and (b) $BaCe_{0.9}Tb_{0.1}O_{3-\delta}$ samples. Solid lines correspond to the fitting results using Eq. (9).

at pO_2 values lower than 10^{-5} atm is attributed to ionic conduction. Consequently, the total conductivity in these conditions can be approximated by the classical model:

$$\sigma_t = \sigma_i + \sigma_p^o(pO_2)^{1/4} \quad (9)$$

where σ_i and σ_p^o are the values of ionic and partial p-type electronic conductivities at unit oxygen pressure. This model was used for fitting the σ vs. pO_2 curves (Fig. 13a).

Tb-doped sample exhibits a different dependence of conductivity with pO_2 (Fig. 13b). In this case, the total conductivity increases nearly linear with decreasing pO_2 with a slope of about −1/5. This behaviour is attributed to the variation in oxygen vacancy concentration with pO_2 due to gradual reduction of Tb^{4+} to Tb^{3+}. Consequently the ionic conduction is not constant and the total conductivity does not follow the simple model of (Eq. (9)).

4. Conclusions

A freeze-drying method was used to prepare barium cerates powders with different dopants on the B-site of the perovskite structure $BaCe_{0.9}Ln_{0.1}O_{3-\delta}$ with Ln = La, Nd, Sm, Gd, Yb, Tb and Y. All materials crystallize in the same Pmcn space group. The lattice cell volume decreases as the ionic radius of the dopant decreases as expected for a solid solution. Only Tb-doped sample shows a different behaviour due to the presence of mixed Tb^{3+} and Tb^{4+} ions in the structure as confirmed by XPS analysis and impedance spectroscopy. Goldschmidt tolerance factor and free volume indicated that Gd is the best dopant for optimizing oxygen ion conductivity in $BaCeO_3$-based materials. Dense ceramic pellets with similar microstructure for all materials were obtained after sintering at 1400 °C. The main difference in the microstructure is the average grain size, which decreases as the ionic radius of the dopant is getting smaller. The bulk, grain boundary and total conductivities of these materials were studied by impedance spectroscopy as a function of the rare-earth doping. The values of the bulk and grain boundary conductivities vary with the rare-earth size, reaching a maximum for Gd-doped samples. This result contradicts the commonly accepted belief that Y-doping is the best option for optimising the ionic conduction in $BaCe_{0.9}Ln_{0.1}O_{3-\delta}$ system.

Acknowledgement

This work was supported by the Spanish (MAT2007-60127) and Canary Islands (PI2007/020) Research programs.

Appendix A. Supplementary data

Supplementary data associated with this article can be found, in the online version, at doi:10.1016/j.jpowsour.2010.11.120.

References

[1] H. Iwahara, H. Uchida, K. Ono, K.J. Ogaki, J. Electrochem. Soc. 135 (1988) 529.
[2] H. Iwahara, Solid State Ionics 86–88 (1996) 9.
[3] K.D. Kreuer, Annu. Rev. Res. 33 (2003) 333.
[4] T. Norby, Solid State Ionics 125 (1999) 1.
[5] N. Bonanos, K.S. Knight, B. Ellis, Solid State Ionics 79 (1995) 161.
[6] T. Schober, Solid State Ionics 162–163 (2003) 277.
[7] N. Bonanos, Solid State Ionics 53–56 (1992) 967.
[8] H. Iwahara, Y. Asakura, K. Katahira, M. Tanaka, Solid State Ionics 168 (2004) 299.
[9] L. Bi, S. Zhang, S. Fang, L. Zhang, K. Xie, C. Xia, W. Liu, Electrochem. Commun. 10 (2008) 1005.
[10] N. Maffei, L. Pelletier, A. McFarlan, J. Power Sources 136 (2004) 24–29.
[11] J. Guan, S.E. Dorris, U. Balachandran, M. Liu, J. Electrochem. Soc. 145 (1998) 1780.
[12] W. Suksamai, I.S. Metcalfe, Solid State Ionics 178 (2007) 627.
[13] R.C.T. Slade, N. Singh, Solid State Ionics 61 (1993) 111.
[14] R.C.T. Slade, N. Singh, Solid State Ionics 46 (1991) 111.
[15] H. Iwahara, T. Yajima, H. Ushida, Solid State Ionics 70–71 (1994) 267.
[16] D. Shima, S.M. Haile, Solid State Ionics 97 (1997) 443.
[17] F.L. Chen, O. Toft Sørensen, G.Y. Meng, D.K. Peng, J. Eur. Ceram. Soc. 18 (1998) 1389.
[18] N. Bonanos, B. Ellis, K.S. Knight, M.N. Mahmood, Solid State Ionics 35 (1989) 179.
[19] G. Ma, T. Shimura, H. Iwahara, Solid State Ionics 120 (1998) 51.
[20] A.N. Virkar, H.S. Maiti, J. Power Sources 14 (1985) 295.
[21] E. Gorbova, V. Maragou, D. Medvedev, A. Demin, P. Tsiakaras, J. Power Sources 181 (2008) 207.
[22] K.H. Ryu, S.M. Haile, Solid State Ionics 125 (1999) 355.
[23] M. Amsif, D. Marrero-López, A. Magrasó, J. Peña-Martínez, J.C. Ruiz-Morales, P. Núñez, J. Eur. Ceram. Soc. 29 (2009) 131.
[24] D. Marrero-López, J. Peña-Martínez, D. Pérez-Coll, P. Núñez, J. Alloys Compd. 422 (2006) 249.
[25] A. El-Himri, D. Marrero-López, P. Núñez, J Solid State Chem. 177 (2004) 3219.
[26] J. Rodríguez-Carvajal, Physica B: Condensed Matter 192 (1993) 55.
[27] Inorganic Crystal Structure Database (ICSD) v2008-02.
[28] R.M. Kwok, XPSPEAK ver. 4.1. XPS Peak Fitting Program for Win 95/98, 2000.
[29] J.C.C. Abrantes, Estereologia, Software Package ESTG/IPVC, Portugal, 2001.
[30] R.D. Shannon, Acta Crystallogr. Sect. A 32 (1976) 751.
[31] V.M. Goldschmidt, Akad. Oslo I. Mater.-Nat. 2 (1926) 7.
[32] http://www.lasurface.com/.
[33] M.V. Rama Rao, T. Shripathi, J. Electron. Spectrosc. Relat. Phenom. 87 (1997) 121.
[34] S. Wang, H. Inaba, H. Tagawa, M. Dokiya, T. Hashimoto, Solid State Ionics 107 (1998) 73.
[35] X. Guo, R. Waser, Prog. Mater. Sci. 51 (2006) 151.
[36] M.N. Rahaman, Y.C. Zhou, J. Eur. Ceram. Soc. 15 (1995) 939.
[37] D. Marrero-López, J. Canales-Vázquez, J.C. Ruiz-Morales, A. Rodríguez, J.T.S. Irvine, P. Núñez, Solid State Ionics 176 (2005) 1807.
[38] Y. Yamazaki, R. Hernandez-Sanchez, S.M. Haile, Chem. Mater. 21 (2009) 2755.
[39] J.E. Bauerle, J. Phys. Chem. Solids 30 (1969) 2657.
[40] J.C.C. Abrantes, J.A. Labrincha, J.R. Frade, J. Eur. Ceram. Soc. 20 (2000) 1603.
[41] D. Pérez-Coll, D. Marrero-López, P. Núñez, S. Piñol, J.R. Frade, Electrochim. Acta 51 (2006) 6463.
[42] S.P.S. Badwal, J. Drennan, J. Mater. Sci. 22 (1987) 3231.